Chemical Science

ROYAL SOCIETY OF CHEMISTRY

EDGE ARTICLE

View Article Online
View Journal | View Issue

Cite this: *Chem. Sci.*, 2025, **16**, 19436

All publication charges for this article have been paid for by the Royal Society of Chemistry

Insights into interfacial water and key intermediates on $Cu_{95}Co_5$ aerogels for electrocatalytic nitrate-to-ammonia conversion

Ming Mu,[a] Junjie Chen,[ab] Xiangxin Xue,[c] Yumei Yang,[a] Ruikai Qi,[d] Yuezhu Wang,[d] Di Liu,[a] Lijia Shang,[a] Wenji Jiang,[a] Xinyi Shao,[a] Zheng-jie Chen,*[e] Bing Zhao[a] and Wei Song*[a]

Received 24th June 2025
Accepted 5th September 2025

DOI: 10.1039/d5sc04633e

rsc.li/chemical-science

Electrocatalytic nitrate reduction (NO_3RR) to ammonia presents a sustainable route for pollutant remediation and green synthesis, yet challenges persist in achieving high efficiency and selectivity. Herein, we report a cobalt-doped copper aerogel ($Cu_{95}Co_5$) synthesized *via* one-step co-reduction, demonstrating exceptional NO_3RR performance with 94.91% faradaic efficiency at −0.6 V and 31.15 mg per mg_{cat} per cm^2 per h NH_3 yield at −0.7 V *vs.* RHE. The system achieves an impressive energy efficiency of 31.03% and enables a record-low ammonia production cost of $0.53 per kg. Multiscale characterization reveals that Co doping induces lattice contraction, optimizes d-band positioning, and enhances interfacial $K^+ \cdot H_2O$ interactions, collectively promoting water dissociation and *H generation. The combination of *operando* spectroscopies (SERS, ATR-FTIR, DEMS) and density functional theory (DFT) calculations elucidates a stepwise hydrogenation pathway: $*NO_3 \rightarrow *NO_2 \rightarrow *NO \rightarrow *NH_2OH \rightarrow *NH_3$, with the rate-determining step (RDS) identified as *NO hydrogenation to *NHO. The hierarchical porosity of the aerogel facilitates mass transport while Cu–Co synergy suppresses hydrogen evolution reactions *via* electronic modulation. Practical viability is demonstrated through stable 12 hour operation in a Zn–NO_3^- battery. This work provides insights into Cu–Co catalysis and establishes design principles for high-performance NO_3RR systems.

Introduction

The pervasive issue of nitrate (NO_3^-) pollution poses a significant threat to aquatic ecosystems and human health, with excessive accumulation in water bodies driving eutrophication and contributing to diseases such as methemoglobinemia and gastric cancer.[1] Annual discharges of nitrate from industrial and agricultural sources exceed millions of tons, while conventional remediation techniques like ion exchange and reverse osmosis suffer from high energy costs and secondary contamination.[1] In recent years, the electrocatalytic nitrate reduction reaction (NO_3RR) has emerged as a transformative strategy, combining pollutant remediation with resource recovery by converting NO_3^- into high-value ammonia (NH_3) through an eight-electron/nine-proton transfer pathway. This process not only enables sustainable NH_3 synthesis but also facilitates energy storage through integration with Zn–NO_3^- battery systems.[2] Compared to the Haber–Bosch process—a century-old industrial method consuming 2% of global energy and emitting 1% of CO_2 annually[3]—NO_3RR leverages the low dissociation energy of N=O bonds (204 kJ mol^{-1}) and the high solubility of NO_3^- (10.4 mol L^{-1}) in water, offering a greener alternative with reduced energy barriers and enhanced economic viability.[4]

Despite the superior NH_3 synthesis activity of noble metals (*e.g.*, Ru, Rh, Pd, Au), their scarcity and high cost drive exploration of earth-abundant transition metal electrocatalysts.[5] Notably, transition-metal alloys, transition-metal oxides, and organometallic compounds (such as transition-metal phthalocyanines and metal–organic frameworks) often exhibit excellent catalytic performance.[6–11] Copper-based catalysts have garnered attention for the NO_3RR due to their unique $3d^{10}4s^1$ electronic configuration. The fully occupied 3d orbitals align energetically with the π* antibonding orbitals of NO_3^-, facilitating electron transfer, while their inherent low hydrogen adsorption energy suppresses competing hydrogen evolution reactions (HERs), thereby enhancing NH_3 selectivity.[12,13] However, monometallic Cu catalysts face challenges such as insufficient active site exposure, limited proton hydrogen supply capacity and sluggish intermediate desorption kinetics. Recent efforts to optimize

[a]State Key Laboratory of Supramolecular Structure and Materials, College of Chemistry, Jilin University, Changchun 130012, PR China. E-mail: weisong@jlu.edu.cn

[b]State Grid Sichuan Electric Power Research Institute, Chengdu, 610041, China

[c]Ministry of Education Key Laboratory of Preparation and Applications of Environmental Friendly Materials, Jilin Normal University, Changchun, 130103, P. R. China

[d]Alan G. MacDiarmid Institute, College of Chemistry, Jilin University, 2699 Qianjin Street, Changchun 130012, PR China

[e]Faculty of Materials Science and Energy Engineering, Shenzhen University of Advanced Technology, Shenzhen, 518107, China. E-mail: zj.chen2@siat.ac.cn

performance *via* stabilizing metastable amorphous structures,[14] oxygen vacancy modulation,[15] and heterostructure construction[16–18] are hindered by complex synthesis protocols, limiting scalability. The introduction of cobalt into Cu-based systems presents a promising solution.[19] Co can also modulate the surface electronic structure of the catalyst by altering the position of the d-band center, thereby optimizing the adsorption strength of intermediates and complementing the NO_3^- activation and deoxygenation capabilities of Cu.[20] Synergistic Cu–Co systems exhibit enhanced catalytic efficiency through electronic and geometric effects. For instance, He *et al.* developed a Cu–Co sulfide-derived core–shell catalyst achieving 93.3% NH_3 faradaic efficiency (FE) in alkaline media, where the Cu/CuO_x core promotes $NO_3^- \rightarrow NO_2^-$ conversion, and the Co/CoO shell accelerates $NO_2^- \rightarrow NH_3$ hydrogenation.[21]

The NO_3RR involves multistep electron transfers and transient intermediates, challenging conventional *ex situ* characterization. *In situ* and quasi *in situ* spectroscopic techniques, including Fourier-transform infrared spectroscopy (FTIR), surface-enhanced Raman spectroscopy (SERS), electron paramagnetic resonance (EPR), and differential electrochemical mass spectrometry (DEMS) offer unprecedented capabilities to probe dynamic interfacial phenomena and resolve molecular vibrations, unpaired electron states, and volatile intermediates at electrified interfaces, unveiling active sites and reaction pathways.[22–24] These atomic-scale insights guide rational design of high-activity/durability catalysts for sustainable ammonia synthesis.

In this work, we synthesize a cobalt-doped copper aerogel ($Cu_{95}Co_5$) *via* a one-step co-reduction method, systematically investigating its NO_3RR performance and mechanism. The material integrates the hierarchical porosity of aerogels—enhancing mass transport and active site accessibility—with Cu–Co electronic synergy, which optimizes the d-band center. $Cu_{95}Co_5$ achieves exceptional performance, delivering 94.91% FE and an NH_3 yield of 31.15 mg mg_{cat}^{-1} cm^{-2} h^{-1} at −0.7 V *vs.* RHE in 1 M KOH. *In situ* surface-enhanced Raman spectroscopy (SERS) reveals elevated interfacial $K^+ \cdot H_2O$ concentrations that accelerate water dissociation and *H generation. The combination of *operando* spectroscopy (SERS, ATR-FTIR, DEMS) and density functional theory (DFT) calculations elucidates a stepwise hydrogenation pathway: $*NO_3 \rightarrow *NO_2 \rightarrow *NO \rightarrow *NH_2OH \rightarrow *NH_3$, with the rate-determining step (RDS) identified as *NO hydrogenation to *NHO. Furthermore, $Cu_{95}Co_5$ demonstrates >12 h stable power output in a Zn–NO_3^- battery, underscoring its practical viability. This study elucidates the electronic structure modulation and interfacial kinetics governing Cu–Co synergy, providing a framework for designing high-performance NO_3RR catalysts. These insights advance the rational development of electrocatalytic ammonia synthesis technologies toward industrial scalability.

Results and discussion

Morphological and structural characterization

The 5% Co-doped Cu aerogel ($Cu_{95}Co_5$ aerogel) was synthesized *via* a co-reduction method, as illustrated in Fig. 1a. Specifically, $CuCl_2$ and $CoCl_2$ aqueous solutions were used, followed by dropwise addition of $NaBH_4$ solution. After 4 hours of static aging at room temperature, the resulting product underwent thorough washing and freeze-drying processes. As revealed by scanning electron microscopy (SEM) in Fig. 1b, the obtained $Cu_{95}Co_5$ aerogel exhibits a three-dimensional porous architecture comprising interconnected nanoparticles. The interconnected nanoporous networks facilitate rapid mass adsorption and transport. Comparative analysis with pure Cu and Co aerogels (Fig. S1 and S2) demonstrates that Co doping significantly modifies the morphological features, yielding a reduced average particle diameter of 45 nm for $Cu_{95}Co_5$, compared to 62.5 nm for pure Cu and 75 nm for pure Co aerogels. This notable size reduction suggests that cobalt incorporation induces lattice strain that influences nanoparticle growth dynamics.[25] High-resolution transmission electron microscopy (HRTEM) analysis in Fig. 1c provides direct evidence of lattice parameter modifications. The measured interplanar spacing of 0.2188 nm corresponds to the (111) plane of face-centered cubic (fcc) Cu, representing an 11.22% contraction compared to standard Cu (0.2465 nm). Considering the slight difference in the atomic radius between Cu (0.1278 nm) and Co (0.1253 nm), the resulting lattice distortion suggests that Co atoms are successfully incorporated into the Cu matrix, giving rise to a locally compressed Cu lattice environment.

Selected-area electron diffraction (SAED) patterns (Fig. 1d) confirm the coexistence of multiple crystalline phases, displaying diffraction rings indexed to CuO (111), Cu (111), Cu (200), Cu (220) and Cu (311) planes. X-ray diffraction (XRD) analysis (Fig. 1e) further elucidates the structural evolution. The pure Cu aerogel exhibits characteristic peaks for both metallic Cu (111, 200, 220) and CuO (111), while the Co aerogel shows weak Co (111) diffraction intensity, suggesting poor crystallinity. Remarkably, the $Cu_{95}Co_5$ aerogel pattern displays exclusively metallic Cu phases, indicating enhanced phase purity through Co doping. Notably, the Cu (111) peak position (42.8°) in the $Cu_{95}Co_5$ aerogel resides between those of the pure Cu aerogel (43.3°) and Co aerogel (44.1°), with all diffraction peaks showing systematic high-angle shifts compared to the pure Cu aerogel. This continuous peak shifting, accompanied by peak broadening, confirms lattice contraction induced by coherent incorporation of smaller Co atoms into the Cu matrix. Elemental distribution analysis through energy-dispersive X-ray spectroscopy (EDS) mapping (Fig. 1f) demonstrates homogeneous dispersion of Co species throughout the Cu matrix, as further supported by the EDS spectrum (Fig. S3). The absence of Co-rich clusters in EDS maps combined with uniform elemental distribution validates the formation of a solid solution structure rather than phase-segregated composites. Quantitative ICP-AES measurement (Fig. 1g and Table S1) confirms the actual Cu : Co ratio as 95.56 : 4.44, closely matching the nominal composition. Valence band spectroscopy (VBS) of X-ray photoelectron spectroscopy (XPS), exhibiting particular sensitivity to d-orbitals near the Fermi level, enables reliable determination of the d-band center (E_d) through weighted averaging of background-subtracted spectral intensity (Shirley method).[26,27] As shown in Fig. 1h, the $Cu_{95}Co_5$ aerogel demonstrates a notable E_d upshift of +0.03 eV *versus* pure Cu and +0.2 eV *versus* Co aerogels. This

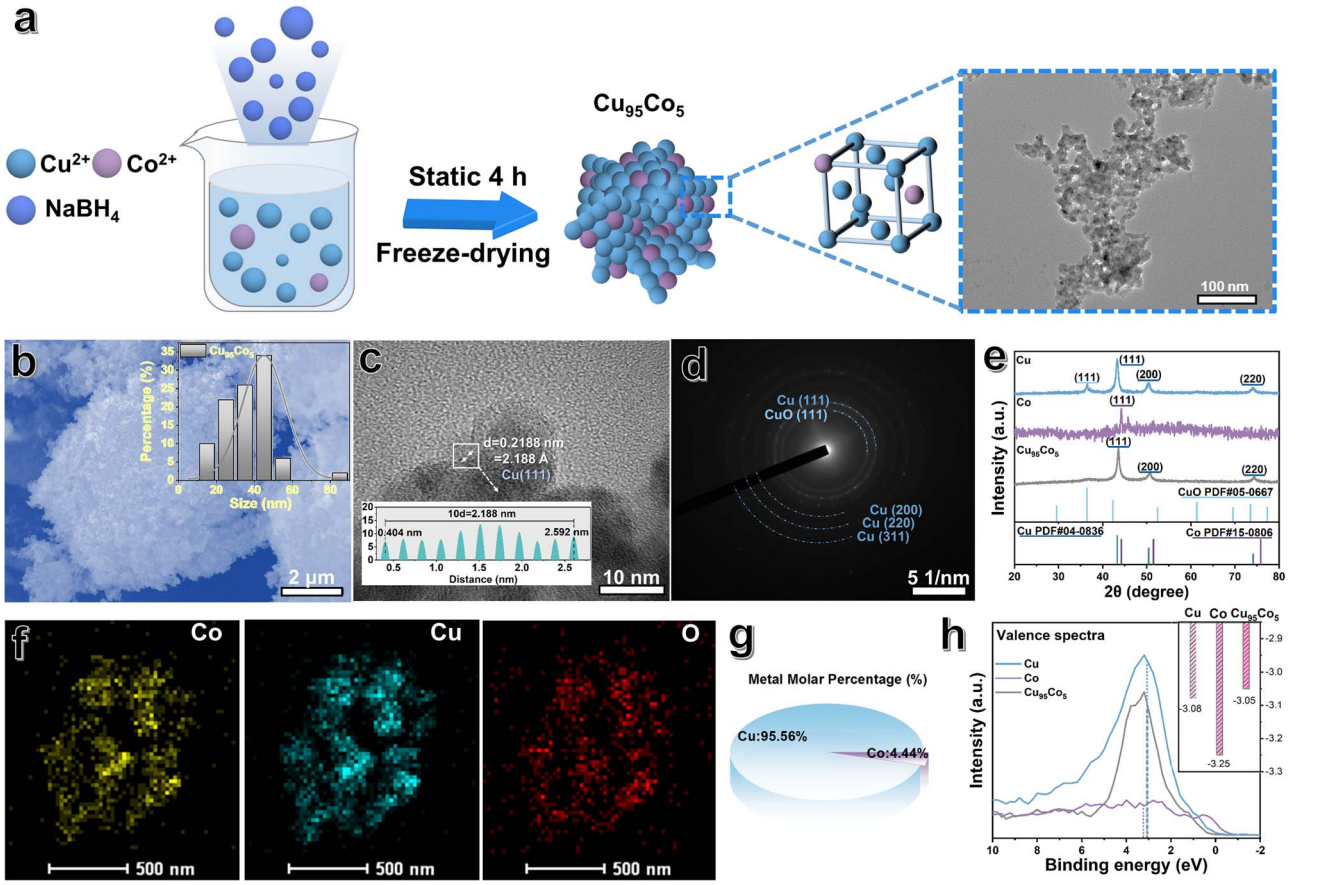

Fig. 1 Characterization of the $Cu_{95}Co_5$ aerogel. (a) Schematic illustration of the synthesis route of the $Cu_{95}Co_5$ aerogel. (b) TEM image of the $Cu_{95}Co_5$ aerogel. (c) HRTEM image of the $Cu_{95}Co_5$ aerogel. (d) Selected area electron diffraction (SAED) pattern of the $Cu_{95}Co_5$ aerogel. (e) XRD patterns of the Cu aerogel, Co aerogel and $Cu_{95}Co_5$ aerogel. (f) EDS mapping of the $Cu_{95}Co_5$ aerogel, showing the spatial distribution of Co (yellow), Cu (green) and O (red). (g) Pie chart of the metal molar percentage of the $Cu_{95}Co_5$ aerogel measured by ICP. (h) XPS valence band spectra of Cu, Co, and the $Cu_{95}Co_5$ aerogel and its d-band center.

significant positive shift confirms synergistic electronic restructuring at the catalyst surface, directly attributable to atomic-level Co incorporation into the Cu lattice. The Cu aerogel exhibits characteristic Raman peaks at 271 cm^{-1} ($F_{2g}(1)$ lattice vibrations of Cu–O from defects/disorder in Cu_2O), 399 cm^{-1} (A_g or B_g modes associated with Cu–O bending vibrations in CuO), 478 cm^{-1} (A_g symmetric stretching vibration of Cu–O in CuO) and 728 cm^{-1} (Cu–OH bending, likely from residual hydroxides during freeze-drying) (Fig. S4). The Co aerogel shows a distinct peak at 646 cm^{-1} (A_{1g} symmetric Co–O stretching in Co_3O_4). For the $Cu_{95}Co_5$ aerogel, the peaks at 280 cm^{-1} ($F_{2g}(1)$ Cu–O vibrations in Cu_2O), 331 cm^{-1} (E_g symmetric Co–O stretching in Co_3O_4), and 614 cm^{-1} (A_{1g}/defect-induced Cu_2O modes) confirm Cu–Co lattice interactions and defect-rich structures.[28,29]

Nitrate reduction reaction (NO_3RR) properties

The electrocatalytic activity of the $Cu_{95}Co_5$ aerogel toward the NO_3RR was systematically investigated in a three-electrode H-cell configuration using 1 M KOH and 0.1 M KNO_3 as the electrolyte. Linear sweep voltammetry (LSV) tests (Fig. 2a) revealed significantly enhanced geometric current densities for Cu aerogel, Co aerogel, and $Cu_{95}Co_5$ aerogel catalysts in the presence of KNO_3 compared to the KNO_3 free electrolyte, confirming their preferential NO_3RR activity over the hydrogen evolution reaction (HER). While the onset potential (~0.2 V *vs.* RHE) for the NO_3RR remained comparable between Cu and $Cu_{95}Co_5$ aerogels, Co doping markedly amplified the current density at identical potentials, with this enhancement becoming more pronounced at higher overpotentials. The LSV comparison among the $Cu_{95}Co_5$ aerogel, $Cu_{99}Co_1$ aerogel, and $Cu_{90}Co_{10}$ aerogel is presented in Fig. S5a. A volcano-shaped relationship between Co doping levels (1–10%) and NO_3RR performance was observed (Fig. S5b), where the $Cu_{95}Co_5$ aerogel catalyst exhibited optimal activity, underscoring the critical role of doping concentration in modulating catalytic behavior. Further *iR*-corrected LSV analysis (Fig. S6) confirmed the superior onset potential and current density of the $Cu_{95}Co_5$ aerogel relative to pure Cu and Co aerogels, solidifying its exceptional NO_3RR capability.

XPS analysis (Fig. S7) demonstrates favorable electron redistribution between Co and Cu, and the electron transfer

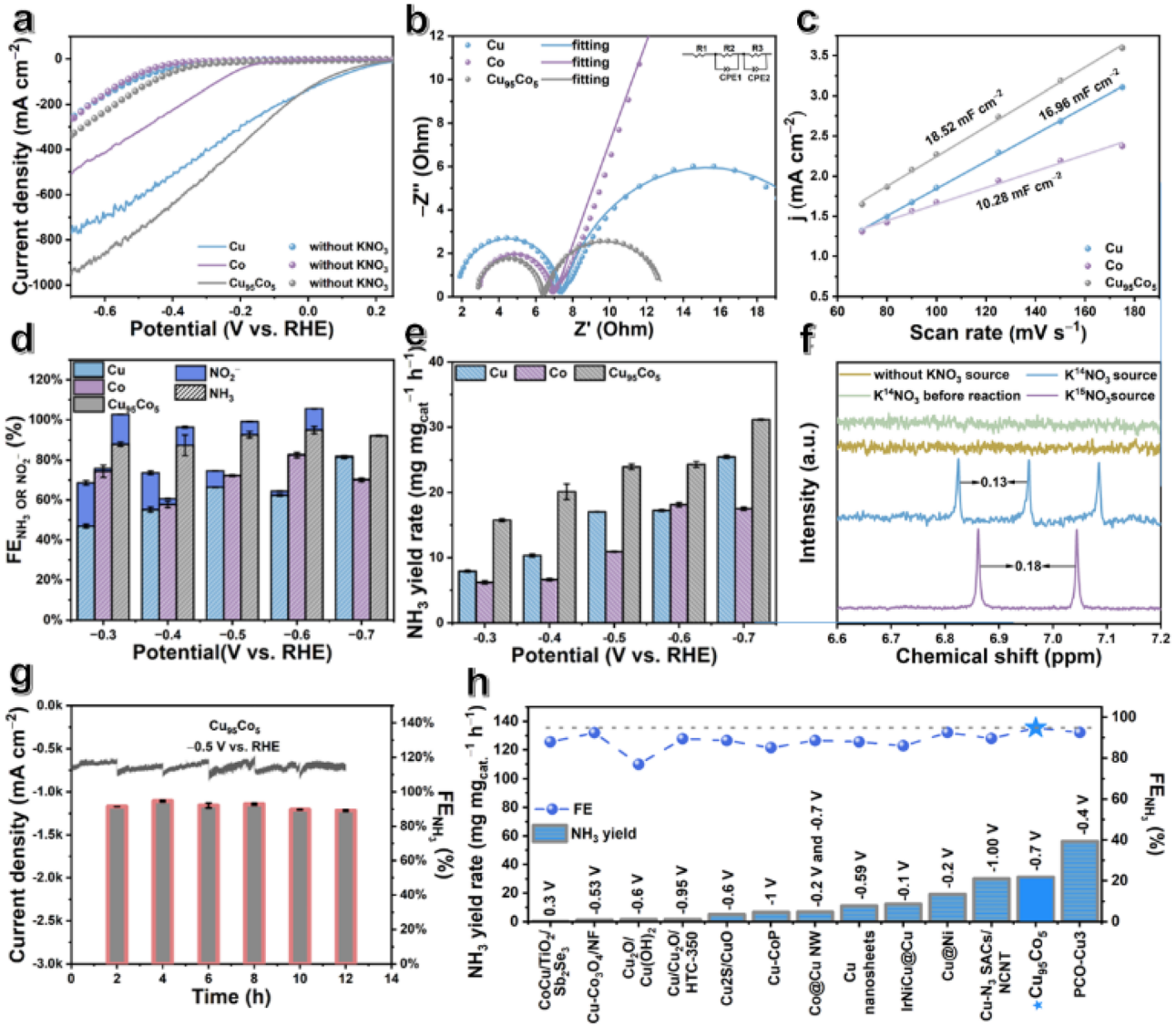

Fig. 2 Electrocatalytic performance of the $Cu_{95}Co_5$ aerogel for NO_3RR conversion. (a) LSV curves of Cu aerogel, Co aerogel, and $Cu_{95}Co_5$ aerogel catalysts in 1 M KOH + 0.1 M KNO_3 (without *IR* compensation). (b) Nyquist plots (EIS) at −1.0 V *versus* Hg/HgO, with an equivalent circuit model. (c) Double-layer capacitance (C_{dl}) derived from capacitive current density ($\Delta j = |j_a - j_c|$) at varying scan rates (70–175 mV s^{-1}). (d) Comparison of FE_{NH_3} and FE_{NO_2} of Cu aerogel, Co aerogel, and $Cu_{95}Co_5$ aerogel catalysts (−0.3 to −0.7 V *vs.* RHE). (e) Comparison of the NH_3 yield rate of Cu aerogel, Co aerogel, and $Cu_{95}Co_5$ aerogel catalysts. (f) ^1H NMR spectra of the products produced after the electrocatalytic NO_3RR of the $Cu_{95}Co_5$ aerogel in the electrolyte of 1 M KOH without KNO_3 (yellow line). ^1HNMR spectra of the fresh electrolytes before electrocatalytic reduction (marked as $^{14}NO_3^-$) were provided as controls (green line). ^1H NMR spectra of the products produced after the electrocatalytic NO_3RR of the $Cu_{95}Co_5$ aerogel in the electrolyte of 1 M KOH with 0.1 M $K^{15}NO_3$ and 0.1 M $K^{14}NO_3$ at −0.7 V (V *vs.* RHE) (blue and purple lines). (g) Cyclic stability test: FE_{NH_3} and NH_3 yield rates over 12 hours (6 cycles, 2 h per cycle) with electrolyte replenishment every 2 h. (h) Comparison of the NH_3 yield rate of the $Cu_{95}Co_5$ aerogel at the potential of −0.7 V (V *vs.* RHE) for 1 h of electrocatalytic NO_3RR with other reported catalysts.

from Co to Cu facilitates interfacial charge transport. XPS quantification (Tables S2 and S3) shows a gradual decrease in the Co^0/Co ratio, and increase in Cu^+ or the Cu^0/Cu ratio. The higher Co doping levels suggest that Co incorporation effectively modifies the electronic environment of Cu, which modulates the d-band center and optimizes the adsorption energy of reaction intermediates, thereby enhancing catalytic performance. Electrochemical impedance spectroscopy (EIS) analysis (Fig. 2b) reveals that the $Cu_{95}Co_5$ aerogel exhibits the lowest charge transfer resistance (R_{ct}) among the catalysts. Moreover, the $Cu_{95}Co_5$ aerogel maintains the smallest R_{ct} compared to the $Cu_{99}Co_1$ aerogel and $Cu_{90}Co_{10}$ aerogel (Fig. S8), indicating optimized reaction kinetics. Tafel slope analysis (Fig. S9) shows that $Cu_{95}Co_5$ exhibits a slope of 165 mV dec^{-1}, lower than those of pure Cu (263 mV dec^{-1}) and Co (275 mV dec^{-1}) aerogels, indicating accelerated reaction kinetics through Co-induced electronic modulation. It synergistically enhances NO_3RR activity by accelerating charge transfer and optimizing intermediate adsorption energetics.[28]

Cyclic voltammetry (CV) measurements at varying scan rates (70–175 mV s^{-1}) enabled determination of double-layer capacitance (C_{dl}, Fig. S10), with the $Cu_{95}Co_5$ aerogel exhibiting the

highest C_{dl} value (18.52 mF cm^{-2}) compared to Cu (16.96 mF cm^{-2}), Co (10.28 mF cm^{-2}), $Cu_{99}Co_1$ (8.54 mF cm^{-2}), and $Cu_{90}Co_{10}$ (15.69 mF cm^{-2}) aerogels (Fig. 2c and S11).[30] This indicates an enlarged electrochemically active surface area (ECSA) due to Co incorporation, consistent with reduced nanoparticle sizes observed in SEM analysis. ECSA-normalized current densities (Fig. S12) revealed that the $Cu_{95}Co_5$ aerogel maintains high intrinsic activity second only to the $Cu_{99}Co_1$ aerogel, suggesting its performance enhancement arises from both increased active site exposure and optimized electronic properties.

Chronoamperometric (CA) tests were performed at applied potentials ranging from −0.3 to −0.7 V *vs.* RHE for 1 hour in 40 mL of 0.1 M KNO_3 + 1.0 M KOH electrolyte to evaluate NH_3 production rates and faradaic efficiency (FE). Current–time profiles are provided in Fig. S13. Quantitative analysis of NO_2^- and NH_3 concentrations was conducted *via* UV-vis spectroscopy using calibration curves (Fig. S14 and S15), while residual NO_3^- levels were determined *via* NO_3^- calibration curves (Fig. S16 and S17). Product distribution analysis revealed that the $Cu_{95}Co_5$ aerogel achieves >50% NH_4^+ selectivity across a broad potential window (−0.3 to −0.7 V *vs.* RHE), reaching near-unity selectivity (∼100%) at −0.6 V (Fig. S17a). The catalyst demonstrates exceptional FE_{NH_3} values exceeding 85% over the entire tested range, peaking at 94.91 ± 0.018% at −0.6 V, significantly outperforming the $Cu_{99}Co_1$ aerogel and $Cu_{90}Co_{10}$ aerogel (Fig. 2d and S18a). Notably, the $Cu_{95}Co_5$ aerogel delivers superior NH_3 yields compared to all control catalysts (Cu aerogel, Co aerogel, $Cu_{99}Co_1$ aerogel and $Cu_{90}Co_{10}$ aerogel) at all potentials (Fig. S18b), achieving a remarkable production rate of 31.15 ± 0.086 mg mg_{cat}^{-1} cm^{-2} h^{-1} at −0.7 V (Fig. 2e). A peak energy efficiency (EE) of 31.03 ± 0.0039% was achieved for NH_3 synthesis over the $Cu_{95}Co_5$ aerogel, at an applied potential of −0.3 V *versus* RHE (Fig. S19). With the nitrate reduction reaction (NO_3RR) advancing toward industrial implementation,[31] the cost of ammonia (NH_3) production has become a key performance metric with significant economic implications. Based solely on the cost of renewable electricity ($0.03 per kWh), the $Cu_{95}Co_5$ aerogel catalyst enables an energy consumption of 17.82 ± 0.22 kWh kg^{-1} NH_3, corresponding to a remarkably low production cost of US $0.53 ± 0.0066 per kg NH_3—substantially below the current commercial price of NH_3 (approximately $1.0–1.5 per kg). In addition, raw material cost estimation suggests that the $Cu_{95}Co_5$ aerogel can be synthesized at a cost of less than $1300 per kilogram, further underscoring its economic advantage over noble-metal-based catalysts. This substantial cost advantage highlights the economic viability of the electrocatalytic NO_3RR as a sustainable alternative to the traditional Haber–Bosch process. Moreover, long-term chronoamperometry tests reveal that the catalyst exhibits a stable lifetime of at least 36 h (Fig. S20). It should be noted that this cost estimation is simplified, considering electricity price only, and does not account for capital expenditures or ohmic losses. Nevertheless, when combined with the environmental benefits of nitrate remediation, the $Cu_{95}Co_5$ aerogel catalyst emerges as a highly attractive candidate for a scalable and economically competitive NO_3RR. Its EE was further benchmarked against those of recently reported catalysts (Table S4). The NH_3 partial current density j_{NH_3} of the $Cu_{95}Co_5$ aerogel further confirms its enhanced activity (Fig. S20).

We have conducted rigorous control experiments to unequivocally confirm the origin of NH_3: ^1H NMR analysis of post-electrolysis KNO_3-free electrolyte (1 M KOH, −0.7 V *vs.* RHE, 1 h) showed no NH_3 signal, confirming that NH_3 formation absolutely requires NO_3^- as the reactant (Fig. S21). ^1H NMR spectra of products from the ^{15}N isotope labeled $^{15}NO_3^-$ electrolyte exhibit the characteristic doublet of $^{15}NH_3$, while the $^{14}NO_3^-$ electrolyte yields the triplet of $^{14}NH_3$ (Fig. 2f). This definitively traces the nitrogen source to electrolyte-derived NO_3^-, eliminating contributions from catalyst decomposition, atmospheric N_2, or environmental contamination.[22]

Cyclic stability tests at −0.5 V *vs.* RHE (6 cycles, 2 h per cycle) demonstrated robust performance retention, with FE_{NH_3} sustained at ∼90% and negligible current density decay (Fig. 2g). Extended 36 hour operation with electrolyte replenishment every 12 h revealed stable NH_3 production (FE > 70%, Fig. S22) we have conducted comprehensive post-electrolysis characterization after both 12 hour and 36 hour chronoamperometry tests, including TEM, XRD, XPS, and ICP analyses to evaluate morphological, structural, and compositional changes. As shown in Fig. S23 (TEM images), the catalyst largely maintained its overall morphology after 12 hours of operation, with no significant structural degradation observed. However, after 36 hours, while the majority of nanoparticles retained their original size and shape, the appearance of needle-shaped nanoparticles indicates certain morphological evolution under extended operation. XRD analysis (Fig. S24) reveals that the characteristic (111), (200), and (220) crystal planes of $Cu_{95}Co_5$ remained intact after both 12 hour and 36 hour tests, confirming the preservation of the bulk crystal structure. After 12 hours, weak CuO (11−1)/(111) peaks emerged (36–37°), suggesting minor surface oxidation in alkaline media. After 36 hours, these CuO peaks intensified while the signal-to-noise ratio decreased, indicating both enhanced surface oxidation and some crystal quality deterioration. XPS analysis (Fig. S25) demonstrates that the Cu/Co oxidation states remained essentially unchanged after 12 hours of operation. After 36 hours, the spectra remained similar. The overall chemical states are well maintained, confirming remarkable structural integrity. ICP results (Fig. S26) show that the Co/Cu ratio decreased slightly from 4.44% to 3.43% after 36 hours, suggesting minor Co leaching during prolonged operation. In summary, these multitechnique analyses demonstrate that the $Cu_{95}Co_5$ aerogel maintains excellent electrochemical and structural stability during 12 hour operation, and largely preserves its fundamental properties even after extended 36 hour testing, with only minimal surface oxidation and negligible Co leaching. As summarized in Fig. 2h and Table S5, the $Cu_{95}Co_5$ aerogel outperforms most previously reported catalysts in both NH_3 yield and FE, attributed to its optimized electronic structure (Co-induced Cu lattice strain) and hierarchical porosity, which synergistically enhance NO_3^- adsorption, intermediate

stabilization, and NH_3 desorption. These results establish the $Cu_{95}Co_5$ aerogel as a benchmark catalyst for efficient nitrate-to-ammonia conversion. And this approach represents a promising strategy for enhancing the performance of NO_3RR catalysts through rational heteroatom doping and nanostructure engineering.

Mechanistic study of catalysts in the NO_3RR

To probe the Cu–Co electronic interplay and its impact on active hydrogen (*H) generation, CV in 1 M KOH revealed distinct hydrogen evolution reaction (HER) features. As shown in Fig. S27a, the $Cu_{95}Co_5$ aerogel exhibits a pronounced HER region below 0.35 V *vs.* RHE, with hydrogen adsorption spanning 0.32 to

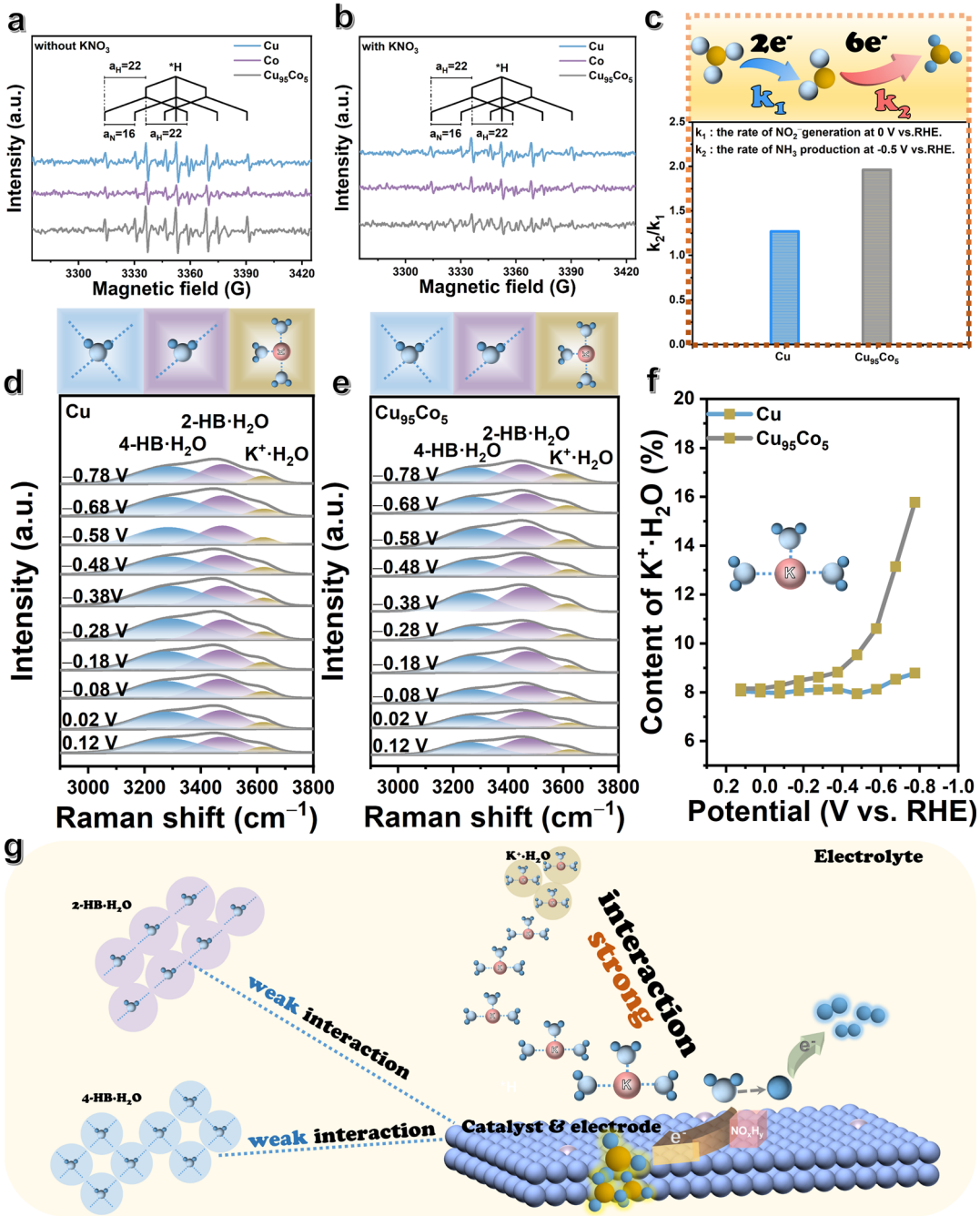

Fig. 3 Characterization of protonic hydrogen in the NO_3RR. (a and b) EPR spectra of the electrolyte for the Cu aerogel, Co aerogel and $Cu_{95}Co_5$ aerogel in 1 M KOH and 1 M KOH with 0.1 M KNO_3. (c) The k_2/k_1 ratios of Cu aerogel and $Cu_{95}Co_5$ aerogel catalysts during the NO_3RR. Potential dependent *in situ* SERS of interfacial water on (d) Cu and (e) $Cu_{95}Co_5$ electrode surfaces during the NO_3RR process. Gaussian fits of three O–H stretching models of 4-HB·H_2O, 2-HB·H_2O, and K^+·H_2O are shown in blue, purple and green. (f) Estimated proportions of K^+·H_2O based on the peak areas of the green bands in the 2900–3800 cm^{-1} Raman spectra on the surfaces of Cu (blue lines) and $Cu_{95}Co_5$ (green lines). (g) Schematic illustration of the mechanism by which the $Cu_{95}Co_5$ aerogel facilitates interfacial water splitting to provide protonic hydrogen, thereby promoting the nitrate reduction reaction.

−0.19 V. Both the Cu aerogel and $Cu_{95}Co_5$ aerogel display similar low-potential hydrogen adsorption (Fig. S27b), whereas Co shows no such activity (Fig. S27c).[32] To quantify *H generation/consumption during the NO_3RR, electrochemical quasi-in situ electron paramagnetic resonance (EPR) measurements were conducted in 1.0 M KOH with/without 0.1 M KNO_3 at −0.6 V *vs.* RHE for 5 min, using 5,5-dimethyl-1-pyrroline *N*-oxide (DMPO) as a spin trap. In a KNO_3^-free electrolyte, the $Cu_{95}Co_5$ aerogel generates a nine-line EPR spectrum (intensity ratio ~ 1 : 1 : 2 : 1 : 2 : 1 : 2 : 2 : 1 : 1, Fig. 3a), characteristic of DMPO–*H adducts, confirming efficient *H production *via* water dissociation. As shown in Fig. 3b, the monometallic Cu aerogel and Co aerogel exhibit weaker signals, indicating inferior HER activity. Upon introducing 0.1 M KNO_3, the $Cu_{95}Co_5$ aerogel shows a marked reduction in DMPO–*H signal intensity, attributed to rapid *H consumption by NO_3RR intermediates, thereby promoting stepwise NO_3^- hydrogenation. In contrast, the relatively small signal attenuation observed for monometallic catalysts indicates their lower *H utilization efficiency. This limitation is most likely associated with their restricted ability to supply proton-derived hydrogen species, which hinders the effective formation and participation of reactive hydrogen intermediates during catalysis. These results underscore that Cu–Co synergy enhances *H generation efficiency and facilitates its dynamic transfer to reaction intermediates, accelerating NO_3^- to NH_3 kinetics and improving overall NO_3RR selectivity. The tailored electronic structure of the $Cu_{95}Co_5$ aerogel optimizes *H availability while suppressing the competitive HER, establishing a mechanistic foundation for its superior catalytic performance.

Kinetics

Comparative linear sweep voltammetry (LSV) of the NO_3RR and NO_2RR (Fig. S28) revealed a negative shift in the onset potential for Cu (−0.04 V *vs.* RHE) and $Cu_{95}Co_5$ (−0.04 V) compared to Co (−0.13 V), indicating Co's inferior $NO_3^- \rightarrow NO_2^-$ kinetics. Product analysis (Fig. S29a and b) showed that $Cu_{95}Co_5$ achieves >93% FE_{NH_3} and 40.08 ± 0.82 mg per mg_{cat} per h NH_3 yield in the NO_2RR, outperforming Cu (37.21 ± 0.42 mg mg_{cat}^{-1} h^{-1}) and Co (35.96 ± 0.60 mg mg_{cat}^{-1} h^{-1}). The faradaic efficiency (FE) and product yield at 0 V are shown in Fig. S30. Rate constants (k_1 for $NO_3^- \rightarrow NO_2^-$, k_2 for $NO_2^- \rightarrow NH_3$) quantified *via* electrochemical analysis (Table S6) revealed $Cu_{95}Co_5$'s superior k_2 (0.11 h^{-1} *vs.* 0.07 h^{-1} for Cu). The k_2/k_1 ratio (2.34 for $Cu_{95}Co_5$ *vs.* 1.77 for Cu, Fig. 3c) highlights Co doping's preferential enhancement of $NO_2^- \rightarrow NH_3$ hydrogenation.[24] Concentration-dependent studies (Fig. S31) demonstrated optimal NH_3 yield at 0.1 M NO_3^-, with performance decline at ≥0.2 M due to limited proton supply or altered electron pathways. Below 0.05 M NO_3^-, the balance between the $NO_3^- \rightarrow NO_2^-$ rate and *H availability dictates overall efficiency. Co doping enhances *H generation, optimizing $NO_2^- \rightarrow NH_3$ kinetics while Cu sites stabilize intermediates. This synergy enables efficient eight-electron conversion (94.91 ± 0.018% FE, 31.15 ± 0.086 mg mg_{cat}^{-1} h^{-1}), establishing the $Cu_{95}Co_5$ aerogel as a benchmark catalyst for nitrate-to-ammonia electrocatalysis.

$K^+ \cdot H_2O$ regulation

In an alkaline electrolyte, the protons (H^+) required for the nitrate reduction reaction (NO_3RR) primarily originate from the interfacial water adsorbed on the surface of the catalyst.[32–34] To further explore how Co doping imparts superior NO_3RR kinetics to the $Cu_{95}Co_5$ catalyst compared to the monometallic Cu, we employed *in situ* SERS (Fig. 3d and e) to analyze the interfacial water structure on the Cu aerogel and $Cu_{95}Co_5$ aerogel electrode surfaces (the schematic diagram of the *in situ* electrochemical testing reactor is presented in Fig. S32). Through Gaussian fitting, we resolved the interfacial water into three components—bonded water (4-HB·H_2O), bi-coordinated hydrogen-bonded water (2-HB·H_2O), and hydrated potassium ion water ($K^+ \cdot H_2O$)—and compared their distributions on the $Cu_{95}Co_5$ surface with those on monometallic Cu. Among them, $K^+ \cdot H_2O$, which forms weak hydrogen bonds with 2-HB·H_2O, is more easily dissociated, thereby accelerating proton transfer. Fig. 3f shows the variation of $K^+ \cdot H_2O$ content with potential at the interfaces of Cu aerogel and $Cu_{95}Co_5$ aerogel catalysts (potential-dependent content of interfacial water components from *in situ* Raman spestroscopy of Cu and $Cu_{95}Co_5$ aerogels are presented in the SI, Fig. S33). $K^+ \cdot H_2O$ is closely related to both the water dissociation ability and the generation of active hydrogen (H*). The results indicate that, on the $Cu_{95}Co_5$ aerogel catalyst surface, the proportion of $K^+ \cdot H_2O$ increases significantly from 8.15% to 15.78%. In contrast, on the Cu aerogel catalyst surface, the content of $K^+ \cdot H_2O$ remains relatively low and shows minimal change, increasing slightly from 8.05% to 8.79%. This comparison suggests that, compared to the Cu aerogel, the $Cu_{95}Co_5$ aerogel has a stronger water dissociation capability, generating more active hydrogen (H*), and the supply rate of H* is more closely matched with the rate of the $NO_3^- \rightarrow NO_2^-$ reaction.[15,27] Additionally, as shown in the SI, Fig. S34, the Raman peak of $K^+ \cdot H_2O$ also shows a more pronounced low-wavenumber shift for $Cu_{95}Co_5$ compared to Cu, further proving that $K^+ \cdot H_2O$ at the $Cu_{95}Co_5$ aerogel interface is subject to stronger electronic modulation.[15] During nitrate reduction (NO_3RR), the availability of active hydrogen (*H) plays a pivotal role in determining both the reaction selectivity and the faradaic efficiency (FE). An insufficient *H supply can limit the overall reduction process, while an excessive *H presence may promote competing side reactions, thereby lowering the faradaic efficiency toward ammonia FE_{NH_3}. Moderate Co doping can enhance water dissociation by regulating the interfacial water structure and increasing the concentration of $K^+ \cdot H_2O$, *i.e.*, the concentration of easily disrupted hydrogen bond networks, thereby promoting *H generation and improving catalyst activity (Fig. 3g). This mechanism helps optimize the kinetic matching between the $NO_3^- \rightarrow NO_2^-$ and $NO_2^- \rightarrow {}^*NH_3$ reaction steps, leading to the superior catalytic performance of the $Cu_{95}Co_5$ aerogel in the NO_3RR.

In situ probing of NO_3RR pathways

Differential electrochemical mass spectrometry (DEMS) was employed to monitor key reaction intermediates during the electrocatalytic nitrate reduction reaction (NO_3RR) by detecting

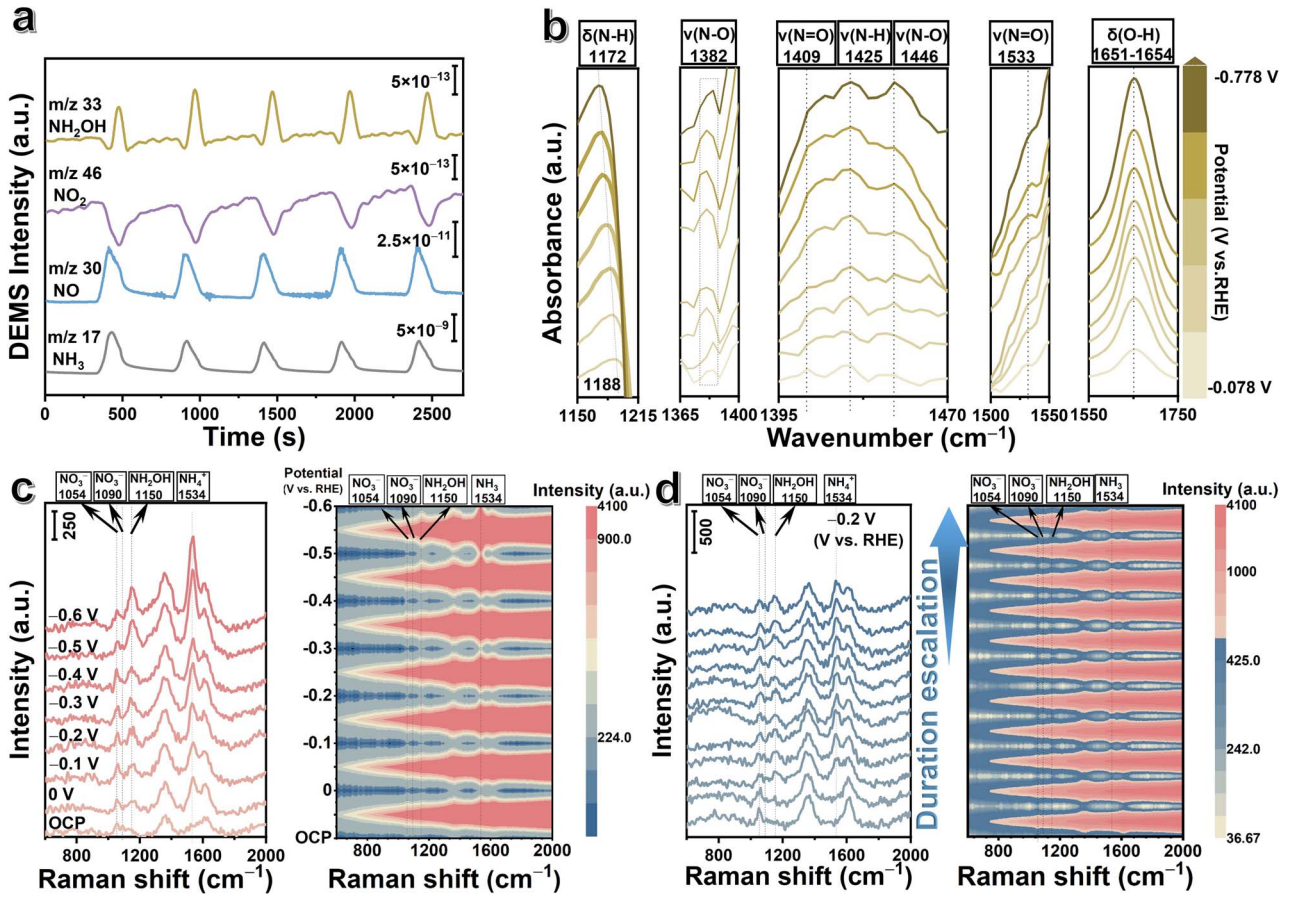

Fig. 4 Characterization of NO_3RR reaction pathways. (a) Electrochemical online DEMS results for the NO_3RR over the $Cu_{95}Co_5$ aerogel. (b) Electrochemical *in situ* ATR-FTIR spectra of the NO_3RR over the $Cu_{95}Co_5$ aerogel at different potentials from −0.078 to −0.778 V *vs.* RHE. (c) *In situ* Raman spectra during the electrocatalytic nitrate reduction process using the $Cu_{95}Co_5$ aerogel as the catalyst, showing changes with negative potential shifts (from 0 to −0.6 V *vs.* RHE) (assignments: δ – bending vibration; ν – stretching vibration; ν_s – symmetric stretching; ν_{as} – asymmetric stretching). The corresponding counter plot is also provided. (d) *In situ* Raman spectra during the electrocatalytic nitrate reduction process using the $Cu_{95}Co_5$ aerogel as the catalyst, showing changes over time. The corresponding counter plot is also provided.

characteristic mass-to-charge ratios (m/z): $m/z = 33$ (NH_2OH), $m/z = 46$ (NO_2), $m/z = 30$ (NO), and $m/z = 17$ (NH_3) (Fig. 4a). The relative intensity of the detected species followed the order: NH_3 > NO > NH_2OH > NO_2, indicating a progressive hydrogenation pathway and consumption of nitrogen-oxygen intermediates. Complementary linear sweep voltammetry (LSV) data (Fig. S35) confirmed the potential-dependent evolution of NH_3, demonstrating a gradual increase in the $m/z = 17$ signal intensity under reductive conditions.[21,25] This trend aligns with the cumulative formation of NH_3 through multi-step proton-coupled electron transfers. These DEMS and LSV results collectively demonstrate the reaction sequence $*NO_3 \rightarrow *NO_2 \rightarrow *NO \rightarrow *NH_2OH \rightarrow *NH_3$, as supported by the temporal evolution of intermediate signals. The dominant NH_3 signal indicates high selectivity toward ammonia formation over competing pathways.

To elucidate the stepwise conversion of $*NO_3$ to $*NH_3$, *in situ* attenuated total reflection Fourier-transform infrared (ATR-FTIR) spectroscopy was conducted over $Cu_{95}Co_5$ aerogel catalysts from −0.078 to −0.778 V *vs.* RHE to resolve the NO_3RR pathway (Fig. 4b). The distinct absorption band at 1172 cm^{-1} is assigned to the N–H bending vibration (δN–H) of adsorbed hydroxylamine ($*NH_2OH$), confirming its pivotal role as a key intermediate. The peak at 1382 cm^{-1} corresponds to the symmetric N–O stretching vibration (ν_sN–O) of surface-adsorbed nitrate ($*NO_3$), indicative of its initial adsorption and activation at Cu sites. Concurrently, the signal at 1409 cm^{-1} is attributed to the N=O stretching vibration (νN=O) of adsorbed nitrite ($*NO_2$), highlighting its role as an early intermediate. The peak at 1425 cm^{-1} arises from the N–H stretching vibration (νN–H) of $*NH_2$ intermediates, while the feature at 1446 cm^{-1} is assigned to the symmetric N–O stretch (ν_sN–O) of $*NO_2$, evidencing its involvement in subsequent deoxygenation steps. Additionally, the absorption band at 1533 cm^{-1} is ascribed to the asymmetric N=O stretching vibration (ν_{as}N=O) of adsorbed *NO or $*NO_2$ species, supporting the progressive reduction of nitrogen-oxygen intermediates. A broad peak near 1651 cm^{-1}, attributed to N–H/O–H bending modes (δN–H/δO–H), likely originates from $*NH_2OH$ or interfacial water molecules, a key intermediate formed through two consecutive

hydrogenation steps of the *NOH species at the nitrogen site. These spectroscopic signatures collectively validate the existence and transformation of critical intermediates (*NO_3, *NO_2, *NO, *NH_2OH) and elucidate a sequential reaction pathway mediated by Cu–Co synergy: (1) nitrate adsorption/activation, (2) stepwise deoxygenation (*NO_3 → *NO_2 → *NO), and (3) hydrogenation (*NO → *NH_2OH → *NH_3).[24,26–28] The Cu sites facilitate nitrate adsorption and initial activation, while Co doping enhances *H transfer efficiency, stabilizing intermediates and accelerating electron transfer. This synergistic interplay optimizes the balance between deoxygenation kinetics and hydrogenation thermodynamics, enabling efficient eight-electron nitrate-to-ammonia conversion.

Complementary to Raman spectroscopy, electrochemical-SERS monitoring was performed using the $Cu_{95}Co_5$ aerogel as the SERS substrate across 600–2000 cm^{-1}. As depicted in Fig. 4c, the distinct peak at 1054 cm^{-1} is assigned to the vibrational mode of adsorbed nitrate (*NO_3), indicative of its adsorption and activation on the catalyst surface. At −0.2 V *vs.* RHE, time-dependent SERS measurements revealed the emergence of three characteristic peaks: 1090 m^{-1} (N–O stretching vibration of *NO_3), 1150 cm^{-1} (N–H bending of *NH_2OH), and 1534 cm^{-1} (N–H stretching of *NH_3). The sequential appearance and intensification of these peaks[22,35,36] confirm the progressive hydrogenation pathway: *NO_3 → *NH_2OH → *NH_3. Potential-dependent *in situ* SERS studies (0 to −0.6 V *vs.* RHE, Fig. 4d) demonstrated that the intensities of 1150 cm^{-1} (*NH_2OH) and 1534 cm^{-1} (*NH_3) peaks increased significantly at more negative potentials, reflecting enhanced intermediate formation and product generation under higher overpotentials.

DFT insights into the NO_3RR mechanism on the $Cu_{95}Co_5$ aerogel

To elucidate the reaction mechanism and the role of Co doping at the atomic level, we performed comprehensive density functional theory (DFT) calculations on the $Cu_{95}Co_5$ system, focusing on the gradual deoxygenation and subsequent hydrogenation steps. As shown in Fig. 5a, the optimized configurations of key intermediates and the corresponding Gibbs free energy profiles reveal that the rate-determining step (RDS) is the hydrogenation of *NO to *NHO. The RDS, defined as the elementary reaction step with the highest energy barrier controlling the overall reaction kinetics, exhibits a significantly lower barrier on $Cu_{95}Co_5$ (0.64 eV) compared to pure Cu (0.92 eV). Further analysis of the *H adsorption free energy (Fig. 5b) demonstrates that $Cu_{95}Co_5$ possesses stronger *H binding affinity than pure Cu, which accounts for the reduced energy barrier during the *NO → *NHO conversion. This computational finding aligns consistently with our *operando* SERS

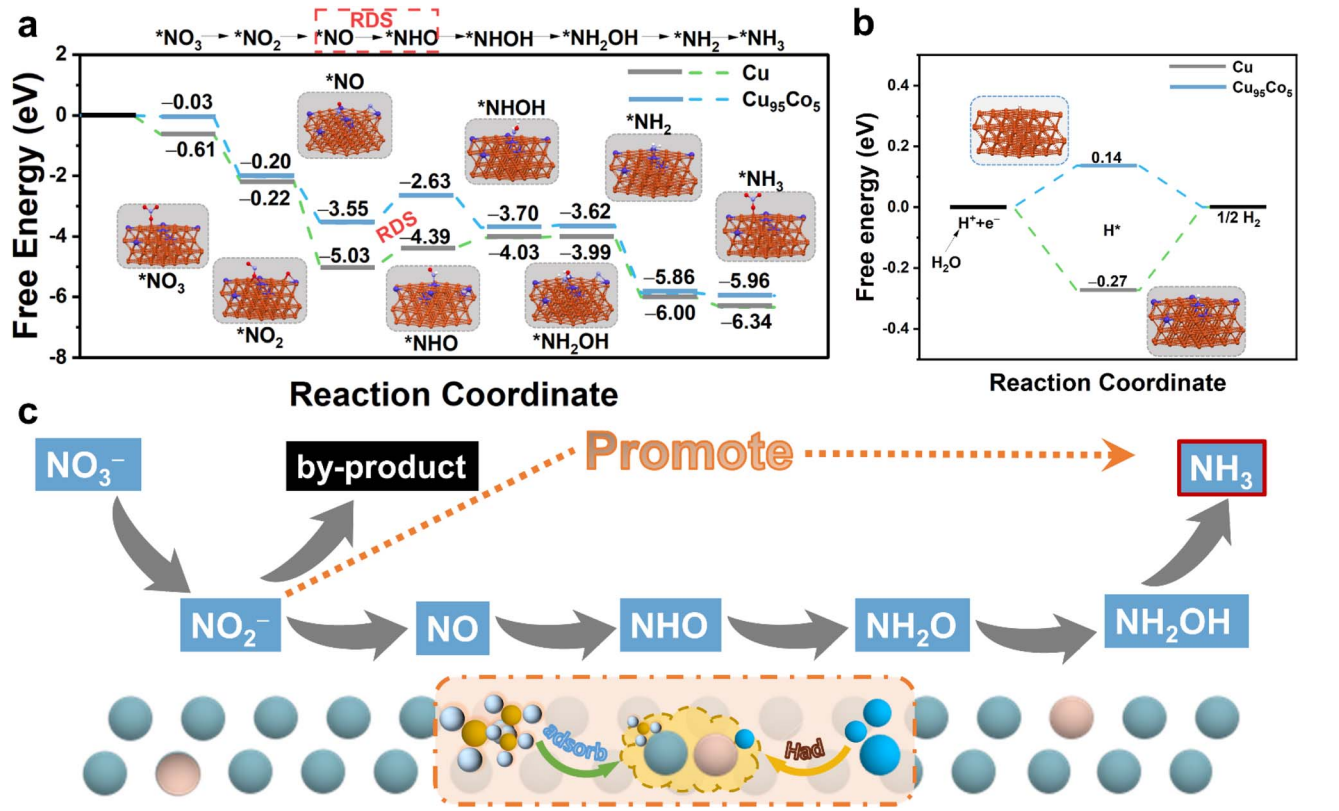

Fig. 5 Density functional theory calculations of the Gibbs free energy diagram for the NO_3^- reduction reaction (NO_3RR) and *H adsorption on the $Cu_{95}Co_5$ surface. (a) Free energy profiles of the NO_3RR intermediate steps (inset: stable adsorption configurations of the reaction intermediates). (b) Free energy profile of *H adsorption on the $Cu_{95}Co_5$ surface. (c) NO_3^- reduction pathway during the NO_3RR using the $Cu_{95}Co_5$ aerogel as the catalyst.

results, which confirmed enhanced interfacial water dissociation and increased *H availability on the Co-doped surface. Integrating these DFT results with multimodal experimental evidence—including DEMS, *in situ* FT-ATIR, ^{1}H NMR, and *in situ* SERS spectroscopy—we propose a synergistic dual-site mechanism (Fig. 5c): NO_3^- is preferentially adsorbed and reduced to NO_2^- on Cu sites, facilitated by favorable electronic interactions, followed by desorption and subsequent hydrogenation on adjacent Co sites. This mechanism, driven by mutual electronic modulation between Cu and Co, enables efficient nitrate-to-ammonia conversion through optimized intermediate stabilization and hydrogenation kinetics.

Zinc-nitrate (Zn–NO_3^-) battery system

The zinc-nitrate (Zn–NO_3^-) battery is an environmentally friendly and efficient clean energy conversion system that can convert NO_3^- in wastewater into high-value products, such as NH_3, while providing power.[2] During the discharge process, zinc dissolves at the anode, while the NO_3RR is catalyzed at the cathode. Since the reduction of NO_3^- to NH_3 involves a complex 8-electron transfer process, this system provides sufficient electron flow to ensure stable battery output and efficient energy utilization. Given the excellent catalytic activity of $Cu_{95}Co_5$ in the NO_3RR, it was used as the cathode, and zinc foil was selected as the anode to construct the Zn–NO_3^- battery shown in Fig. 6a. As shown in Fig. 6b, the Zn–NO_3^- battery with $Cu_{95}Co_5$ as the catalytic cathode exhibits an open-circuit voltage of 1.49 V, which remains stable for 1 hour, indicating good electrochemical stability. Power density is one of the key indicators of battery performance and is crucial for evaluating energy conversion efficiency and practical application potential. As shown in Fig. 6c, the Zn–NO_3^- battery based on $Cu_{95}Co_5$ reaches a maximum power density of 12.40 mW cm^{-2} at 0.35 V (V *vs.* Zn). Additionally, as shown in Fig. 6d, this Zn–NO_3^- battery discharges normally at current densities ranging from 1 mA cm^{-2} to 50 mA cm^{-2}, demonstrating good rate performance (relevant information for Cu and Co can be found in the SI, Fig. S36). At low to medium current densities (1–10 mA cm^{-2}), the battery maintains a high potential (1.35–1.45 V), while at

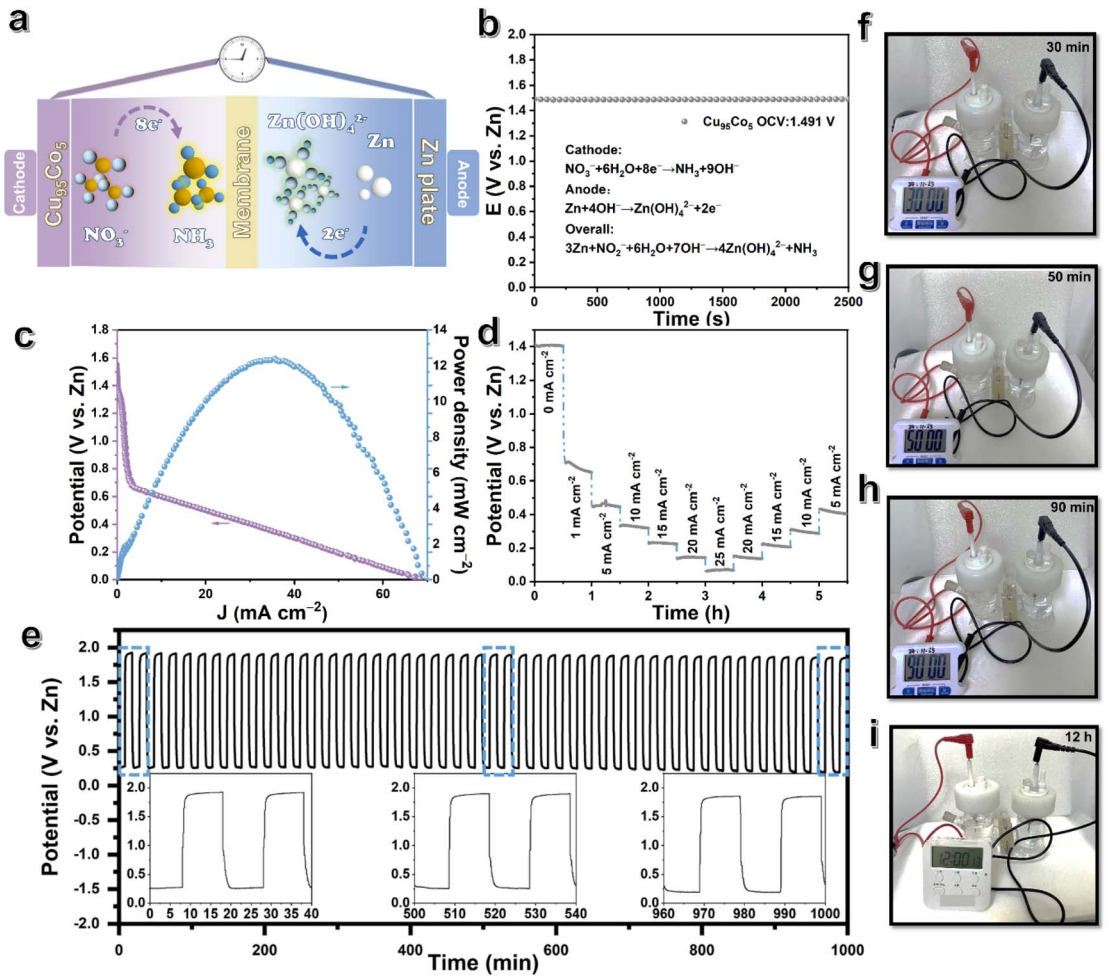

Fig. 6 Zn–NO_3^- battery. NO_3RR-involved rechargeable hybrid battery measurements. (a) Schematic diagram of the rechargeable Zn–NO_3^- battery. (b) Open circuit voltage tests, (c) polarization curve and power density tests, and (d) multi-step chronoamperometric curves of $Cu_{95}Co_5$ aerogel cathodes at various current densities during the discharge process. (e) Long-term cycling stability test of the Zn–NO_3^- battery using the $Cu_{95}Co_5$ aerogel cathode at 2 mA cm^{-2}. (f–i) Photographs of the $Cu_{95}Co_5$ aerogel-based Zn–NO_3^- battery powering an electronic timer.

higher current densities (50 mA cm^{-2}), the potential drops to around 1.10 V, indicating significant polarization. After high-rate discharge, the battery recovers to around 1.40 V, showing good dynamic recovery performance. These results indicate that, despite significant polarization at high current densities, the Zn–NO_3^- battery overall exhibits a high open-circuit voltage, good electrochemical stability, and strong current output capability, providing solid performance support for practical applications. The stability of the Zn–NO_3^- battery based on $Cu_{95}Co_5$ was further evaluated through constant current charge–discharge cycling experiments. As shown in Fig. 6e, at a current density of 2 mA cm^{-2}, the battery remains stable after 50 charge–discharge cycles without significant performance degradation. Additional cycling data (Fig. S37) revealed that the battery could operate continuously for 36 hours without short-circuiting (Fig. S37a), sustain repeated cycling over extended periods (Fig. S37b), and achieve a peak round-trip energy efficiency of 60% in the first 37 hours (~110 cycles), which remained above 50% before declining likely due to nitrate depletion in the electrolyte (Fig. S37c). The system exhibited nearly 100% coulombic efficiency over 140 cycles (Fig. S37d) and maintained a constant areal capacity of 0.334 mA h·cm^{-2} (Fig. S37e), indicating exceptional cycling stability. Compared to other reported NO_3RR-based systems (Table S7), the Zn–NO_3^- battery with the $Cu_{95}Co_5$ cathode demonstrates competitive round-trip efficiency, near-ideal coulombic efficiency, and stable capacity retention. Although gradual efficiency decay was observed over prolonged cycling—attributed to nitrate consumption—the system retained strong electrochemical reversibility and consistent discharge capacity, underscoring its promise as an energy storage technology coupled with nitrate reduction. Furthermore, as shown in Fig. 6f–i, the Zn–NO_3^- battery based on $Cu_{95}Co_5$ is capable of providing continuous power for over 12 hours to a typical electronic timer, indicating stable current output and demonstrating its potential as a power source in practical applications.

Conclusions

This study demonstrates that Co-doped Cu aerogels ($Cu_{95}Co_5$) synthesized *via* a one-step co-reduction method achieve exceptional electrocatalytic nitrate-to-ammonia conversion, with 94.91% faradaic efficiency and 31.15 mg per mg_{cat} per cm^2 per h NH_3 yield at −0.7 V *vs.* RHE. The combination of *operando* spectroscopy (SERS, ATR-FTIR, DEMS) and density functional theory (DFT) calculations elucidates a stepwise hydrogenation pathway: $*NO_3 \rightarrow *NO_2 \rightarrow *NO \rightarrow *NH_2OH \rightarrow *NH_3$, with the rate-determining step (RDS) identified as *NO hydrogenation to *NHO, and Co doping was identified to play pivotal roles: (1) inducing lattice strain (11.22% Cu contraction) that optimizes the d-band center and tunes the adsorption energies of reactants and intermediates at active sites; (2) the incorporation of Co induces an upshift in the d-band center, thereby optimizing the adsorption–desorption kinetics of critical nitrogenous intermediates and promoting superior catalytic performance. (3) Enhancing interfacial $K^+ \cdot H_2O$ interactions to accelerate water dissociation and *H generation; (4) elevating the $NO_2 \rightarrow NH_3$ rate constant (k_2: 48.93% higher than pure Cu) through electronic synergy. The hierarchical porosity of the aerogel facilitated mass transport while suppressing the HER. Practical viability was confirmed *via* a Zn–NO_3^- battery delivering stable power for >12 h. These findings establish Cu–Co aerogels as model systems for sustainable NH_3 synthesis, emphasizing metastable phase engineering and interfacial water modulation as critical design principles for next-generation NO_3RR catalysts.

Author contributions

Ming Mu: conceptualization, experiments, formal analysis, software, writing – original draft. Junjie Chen: conceptualization, investigation. Xiangxin Xue: investigation. Yumei Yang: investigation, formal analysis. Ruikai Qi: investigation. Yuezhu Wang: investigation. Di Liu: formal analysis. Lijia Shang: formal analysis. Wenji Jiang: investigation. Xinyi Shao: investigation. Zheng-jie Chen: DFT calculations. Bing Zhao: resources. Wei Song: supervision, conceptualization, resources, writing – review & editing.

Conflicts of interest

There are no conflicts to declare.

Data availability

Data will be made available on request.

The supplementary materials include detailed information on chemicals, material synthesis and characterization methods, as well as electrochemical measurements and analysis of electrocatalytic products. Additionally, calculations of the VBS d-band center are presented. Relevant figures and tables are also provided to support the findings. See DOI: **https://doi.org/10.1039/d5sc04633e**.

Acknowledgements

This work was supported by the research grants from the National Natural Science Foundation of China (22474048 and 22074051).

References

1 H. Zhang, H. Wang, X. Cao, M. Chen, Y. Liu, Y. Zhou, M. Huang, L. Xia, Y. Wang and T. Li, *Adv. Mater.*, 2024, **36**, 2312746.
2 H. Zhang, K. Fang, J. Yang, H. Chen, J. Ning, H. Wang and Y. Hu, *Coord. Chem. Rev.*, 2024, **506**, 215723.
3 J. Liang, Z. Li, L. Zhang, X. He, Y. Luo, D. Zheng, Y. Wang, T. Li, H. Yan and B. Ying, *Chem*, 2023, **9**, 1768–1827.
4 D.-C. Zhong, Y.-N. Gong, C. Zhang and T.-B. Lu, *Chem. Soc. Rev.*, 2023, **52**, 3170–3214.
5 S. Han, H. Li, T. Li, F. Chen, R. Yang, Y. Yu and B. Zhang, *Nat. Catal.*, 2023, **6**, 402–414.

6 S. Bhowmick, A. Adalder, A. Maiti, S. Kapse, R. Thapa, S. Mondal and U. K. Ghorai, *Chem. Sci.*, 2025, **16**, 4806–4814.
7 S. Sarkar, A. Adalder, S. Paul, S. Kapse, R. Thapa and U. K. Ghorai, *Appl. Catal., B*, 2024, **343**, 123580.
8 N. Mukherjee, A. Adalder, N. Barman, R. Thapa, R. Urkude, B. Ghosh and U. K. Ghorai, *J. Mater. Chem. A*, 2024, **12**, 3352–3361.
9 A. Adalder, S. Paul, N. Barman, A. Bera, S. Sarkar, N. Mukherjee, R. Thapa and U. K. Ghorai, *ACS Catal.*, 2023, **13**, 13516–13527.
10 A. Adalder, K. Mitra, N. Barman, R. Thapa, S. Bhowmick and U. K. Ghorai, *Adv. Energy Mater.*, 2024, **14**, 2403295.
11 U. K. Ghorai, S. Paul, B. Ghorai, A. Adalder, S. Kapse, R. Thapa, A. Nagendra and A. Gain, *ACS Nano*, 2021, **15**, 5230–5239.
12 J. Liu, Z. Li, C. Lv, X.-Y. Tan, C. Lee, X. J. Loh, M. H. Chua, Z. Li, H. Pan and J. Chen, *Mater. Today*, 2024, **73**, 208–2597.
13 Z. Yu, M. Gu, Y. Wang, H. Li, Y. Chen and L. Wei, *Adv. Energy Sustainability Res.*, 2024, **5**, 2300284.
14 Y. Wang, S. Wang, Y. Fu, J. Sang, P. Wei, R. Li, D. Gao, G. Wang and X. Bao, *Nat. Commun.*, 2025, **16**, 897.
15 W. Hiramatsu, Y. Shiraishi, S. Ichikawa, S. Tanaka, Y. Kawada, C. Hiraiwa and T. Hirai, *J. Am. Chem. Soc.*, 2024, **147**, 1968–1979.
16 J. Chen, M. Li, X. Wang, H. Liu, W. Jiang, B. Zhao and W. Song, *Angew. Chem., Int. Ed.*, 2025, **64**, e202424986.
17 D. Liu, P. Duan, J. Chen, M. Mu, Y. Yang, F. Ma, B. Zhao and W. Song, *Laser Photon. Rev.*, 2025, e01214.
18 J. Yu, Y. Liu, C. Fan, N. Liu, J. Yin, Y. Li, Y. Cheng, X. Yuan, X. Zhang, Y. Liu, S. Fan, L. Xu and H. Li, *Nano Res.*, 2025, **18**, e94907135.
19 Y. Cui, C. Sun, G. Ding, M. Zhao, X. Ge, W. Zhang, Y. Zhu, Z. Wang and Q. Jiang, *Sci. China Mater.*, 2023, **66**, 4387–4395.
20 W. Yang, Z. Chang, X. Yu, P. Wu, R. Shen, L. Wang, X. Cui and J. Shi, *Adv. Sci.*, 2025, **12**, 2416386.
21 W. He, J. Zhang, S. Dieckhöfer, S. Varhade, A. C. Brix, A. Lielpetere, S. Seisel, J. R. Junqueira and W. Schuhmann, *Nat. Commun.*, 2022, **13**, 1129.
22 S.-N. Zhang, P. Gao, Q.-Y. Liu, Z. Zhang, B.-L. Leng, J.-S. Chen and X.-H. Li, *Nat. Commun.*, 2024, **15**, 10877.
23 J. Chen, X. Xing, S. Wen, M. Li, W. Jiang, X. Shao, R. Qi, Y. Yang, M. Mu, Z. Chen, B. Zhao and W. Song, *Chem. Eng. J.*, 2025, **521**, 167002.
24 H. Wang, J. Huang, J. Cai, Y. Wei, A. Cao, B. Liu and S. Lu, *Small Methods*, 2023, **7**, 2300169.
25 B. Wang, K. Li, G. Xu, Z. Zhang, X. Wang, J. Sun, Y. Song, X. Zhang, Y. Liang, D. Kong, Y. Qiu, Q. Teng, X. Cui, J. Chen, J. Zhao, J. Wang, H. Yang, J. Huang and Y. Tang, *Angew. Chem., Int. Ed.*, 2025, **64**, e202502725.
26 S. J. Hwang, S.-K. Kim, J.-G. Lee, S.-C. Lee, J. H. Jang, P. Kim, T.-H. Lim, Y.-E. Sung and S. J. Yoo, *J. Am. Chem. Soc.*, 2012, **134**, 19508–19511.
27 X. Wu, F. Chen, N. Zhang, Y. Lei, Y. Jin, A. Qaseem and R. L. Johnston, *Small*, 2017, **13**, 1603387.
28 L. Qiao, A. Zhu, D. Liu, K. An, J. Feng, C. Liu, K. W. Ng and H. Pan, *Adv. Energy Mater.*, 2024, **14**, 124528.
29 H.-Q. Chen, H. Ze, M.-F. Yue, D.-Y. Wei, Y.-L. A, Y.-F. Wu, J.-C. Dong, Y.-J. Zhang, H. Zhang, Z.-Q. Tian and J.-F. Li, *Angew. Chem., Int. Ed.*, 2022, **134**, e202117834.
30 T. Zhang, J. Lv, R. Yang, Z. Yan, X. Sun, X. Xu and Y. Liu, *Adv. Energy Mater.*, 2024, **14**, 2400790.
31 W. Zheng, L. Zhu, Z. Yan, Z. Lin, Z. Lei, Y. Zhang, H. Xu, Z. Dang, C. Wei and C. Feng, *Environ. Sci. Technol.*, 2021, **55**, 13231–13243.
32 J. Yu, R.-T. Gao, X. Guo, N. T. Nguyen, L. Wu and L. J. Wang, *Angew. Chem., Int. Ed.*, 2025, **64**, e202415975.
33 S. J. Zheng, X. Y. Dong, H. Chen, R. W. Huang, J. Cai and S. Zang, *Angew. Chem., Int. Ed.*, 2025, **64**, e202413033.
34 J. Ni, J. Yan, F. Li, H. Qi, Q. Xu, C. Su, L. Sun, H. Sun, J. Ding and B. Liu, *Adv. Energy Mater.*, 2024, **14**, 2400065.
35 Y. Li, Z. Lu, L. Zheng, X. Yan, J. Xie, Z. Yu, S. Zhang, F. Jiang and H. Chen, *Energy Environ. Sci.*, 2024, **17**, 4582–4593.
36 W. Gao, K. Xie, J. Xie, X. Wang, H. Zhang, S. Chen, H. Wang, Z. Li and C. Li, *Adv. Mater.*, 2023, **35**, 2202952.